metals

Article

Deformation Behavior of Sintered Cu-10wt%Mo Composite in the Hot Extrusion Process

Qing Li [1,2,3,*], Zengde Li [2], Zhanning Zhang [2] and Songxiao Hui [2,*]

[1] State Key Laboratory of Nonferrous Structural Materials, GRINM Group Co., Ltd., Beijing 100088, China
[2] GRIMAT Engineering Institute Co., Ltd., Beijing 101407, China
[3] General Research Institute for Nonferrous Metals, Beijing 100088, China
* Correspondence: liqing@grinm.com (Q.L.); huisx@grinm.com (S.H.)

Abstract

A hot extrusion deformation test of sintered Cu-10wt%Mo composite was carried out under deformation conditions, with deformation temperatures ranging from 800 °C to 950 °C, and extrusion ratios ranging from 2.9 to 10.5. The hot extrusion process eliminated the original interfaces between copper powder particles in sintered Cu-10wt%Mo composite. While the copper phase experienced dynamic recrystallization, the molybdenum particles effectively pinned the boundaries and inhibited subsequent grain growth. As the extrusion ratio increased, the composite material's tensile strength, elongation, and thermal conductivity first increased and then decreased. With the rise in hot extrusion deformation temperature, the composite material's tensile strength, elongation, and thermal conductivity gradually increased, but stabilized after reaching 900 °C. Deformation during hot extrusion is confined to the copper phase, which undergoes dynamic recrystallization (DRX), with no significant deformation occurring in the molybdenum phase. The molybdenum phase promotes an increased local strain rate in the copper phase, resulting in the formation of a certain number of twin grains.

Keywords: Cu-10wt%Mo composite; hot extrusion deformation; thermal conductivity; local strain rate; twin grains

1. Introduction

Molybdenum-copper (Mo-Cu) composite consists of molybdenum and copper, in which the two phases are mutually insoluble and do not form intermetallic compounds. Mo-Cu composite combines the advantageous properties of molybdenum, such as high strength, high hardness, corrosion resistance, and a low coefficient of thermal expansion, with the high electrical and thermal conductivity characteristics of copper [1–5]. By adjusting the molybdenum-to-copper ratio, Mo-Cu composites with tailored properties can be produced, making them suitable for widespread applications in electrical contacts, heat sink structural components, and high-temperature components for rockets and missiles [6–11].

Cu-10wt%Mo composite is composed of 10wt% Mo and 90wt%Cu, and the ratio and distribution of the Mo and Cu phases are key determinants of the composite material properties [3,6,11]. When preparing molybdenum copper composite with a molybdenum content exceeding 45%, molybdenum forms a uniformly connected molybdenum skeleton in advance, and the capillary force formed by the gaps between the molybdenum skeletons melts and penetrates copper to form a high-density Mo-Cu composite. Due to its low

Check for updates

Academic Editor: Jiro Kitagawa

Received: 20 November 2025
Revised: 25 December 2025
Accepted: 27 December 2025
Published: 29 December 2025

Copyright: © 2025 by the authors. Licensee MDPI, Basel, Switzerland. This article is an open access article distributed under the terms and conditions of the Creative Commons Attribution (CC BY) license.

molybdenum content, which is insufficient to form a continuous molybdenum skeleton, Cu-10wt%Mo composite cannot be prepared via the powder metallurgy liquid-phase sintering method [12–15]. Cu-10wt%Mo composite can be prepared by the powder metallurgy solid-phase sintering method. The low temperature of solid-phase sintering inhibits the formation of adequate sintering necks between molybdenum and copper powder particles. Consequently, the powders are primarily bonded through mechanical interlocking, which results in composite defects such as low density, high porosity, and overall structural looseness. These defects primarily reside at the interfaces: between Cu-Cu particles, between Mo-Mo particles, and at the hetero-interfaces between Cu and Mo particles. During metal hot extrusion processing, the metal is subjected to strong compressive stresses in the axial, radial, and circumferential directions [16–18]. This pressure state can suppress the generation and propagation of intergranular cracks, improve the plastic processing ability of the material, and also achieve large deformation through a large extrusion ratio.

In this paper, a hot extrusion deformation test of sintered Cu-10wt%Mo composite was carried out under deformation conditions, with deformation temperatures ranging from 800 °C to 950 °C, and extrusion ratios ranging from 2.9 to 10.5. Based on the experimental results, the effects of hot extrusion deformation on the microstructure, mechanical properties, and thermal conductivity of Cu-10wt%Mo composite prepared by powder metallurgy solid-state sintering have been elucidated.

2. Materials and Methods

Cu-10wt%Mo composite was prepared via the powder metallurgy solid-state sintering route, with a nominal composition of 10wt%Mo and 90wt%Cu. Figure 1 shows the flowchart for sample preparation and analysis. The sintered Cu-10wt%Mo composite rod, shown in Figure 2, with a size of D95 mm × 200 mm, was subjected to hot extrusion processing on a non-ferrous metal profile extruder with the model XJ-630(Wuxi Yuanchang Machinery Manufacturing Co., Ltd, Wuxi, China). The rods were heated to the deformation temperature at a speed of 10 °C/s, at a holding time of 70 min at the deformation temperature. The deformation temperatures used in this experiment were 800, 850, 900, and 950 °C; the extrusion ratios were 2.9, 4.7, 7.0, and 10.5. After hot extrusion was completed, the composite material rods were immediately quenched in water to maintain the microstructure morphology after high-temperature deformation.

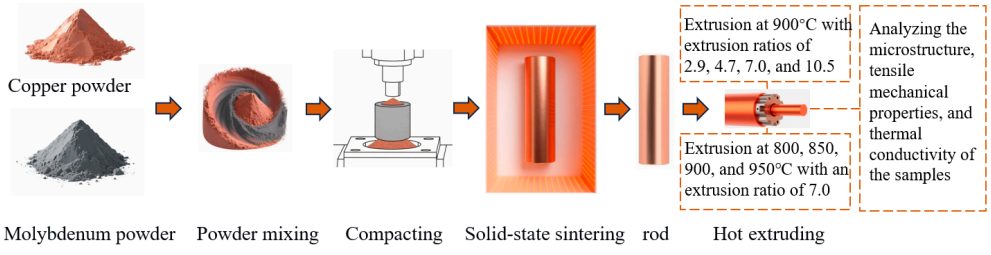


Figure 1. The flowchart for sample preparation and analysis.

The microstructure of the Cu-10wt%Mo composite was analyzed using a HITACHI S4800 scanning electron microscope (Hitachi High-Tech Corporation, Hitachinaka City, Ibaraki Prefecture, Japan) equipped with an EMAX energy-dispersive X-ray spectroscopy (EDS) system and an electron backscatter diffraction (EBSD) detector. The metallographic structure of the chemically etched Cu-10wt%Mo composite was examined using an optical microscope (Olympus Corporation, Tokyo Metropolis, Japan). Tensile tests of the Cu-10wt%Mo composite at 25 °C were conducted on a CMT5105 electronic universal testing machine (MTS Systems Corporation, Eden Prairi, Minnesota, USA) in accordance with GB/T 228.1-2021 [19]. The thermal conductivity of the Cu-10wt%Mo composite was

measured using a JR-3 laser thermal conductivity meter (Changsha Zhongda Precision Instrument Co., Ltd, Changsha, China) in accordance with GB/T 22588-2008 [20]. The tensile mechanical properties and thermal conductivity were both measured in triplicate, and the average values were taken as the final experimental data.

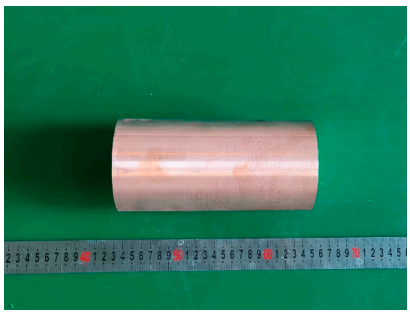


Figure 2. The sintered Cu-10wt%Mo composite rod.

3. Results and Discussion

3.1. Microstructure Evolution

Figure 3 shows representative SEM images of the sintered and subsequently extruded Cu-10wt%Mo composite, where the light blue area represents the molybdenum phase and the yellow area represents the copper phase. It can be seen from Figure 3a that many pores are in the microstructure of the sintered Cu-10wt%Mo composite and the pores exist in the copper phase, molybdenum phase, and copper–molybdenum phase interface of the sintered composite material matrix. As shown in Figure 3b, the extruded Cu-10wt%Mo composite exhibits a microstructure with negligible porosity, which is characteristic of high-density powder metallurgy materials.

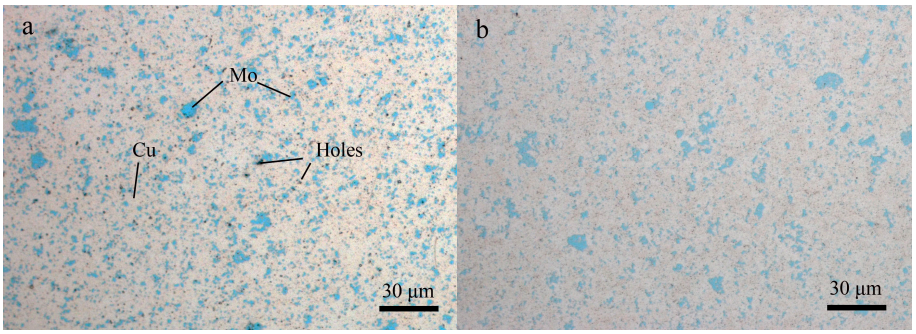


Figure 3. SEM micrographs of the Cu-10wt%Mo composite: (**a**) as sintered and (**b**) after hot extrusion.

Achieving a fully dense Cu-10wt%Mo composite via powder metallurgy solid-phase sintering is challenging, primarily due to the limited interdiffusion and incomplete sintering between the constituent phases. The high temperature and pressure generated during hot extrusion deformation further shrink and close the pores between powder particles in the sintered Cu-10wt%Mo composite, promoting atomic diffusion and the disappearance of the original interfaces between copper powder particles, thereby increasing the density of the material.

Figure 4 compares the microstructures of the Cu-10wt%Mo composite extruded at 900 °C across extrusion ratios of 2.9, 4.7, 7.0, and 10.5, with the molybdenum and copper phases denoted by light blue and gray regions, respectively. Figure 5 presents inverse pole figure (IPF) maps of the Cu-10wt%Mo composite for different extrusion ratios, with the colors corresponding to crystallographic orientations relative to the extrusion direction. The subfigures labeled 1 and 2 represent the matrix copper phase grains and their statistical

distributions, respectively, while subfigures labeled 3 and 4 show those of the molybdenum phase. Figures 4 and 5 reveal that, during hot extrusion with different ratios, dynamic recrystallization consistently occurs in the copper phase of the composite material. The copper grains undergo progressive refinement with increasing extrusion strain. At extrusion ratios of 7.0 and 10.5, dynamic recrystallization yields a refined copper matrix consisting of fine, uniform equiaxed grains with average sizes of 10.11 μm and 10.09 μm, as shown in Figure 5(c_2) and Figure 5(d_2), respectively. The molybdenum phase shows no evidence of deformation-induced elongation, with a stable average grain size of ~1 μm, regardless of the extrusion ratio (Figure 5(a_4–d_4)).

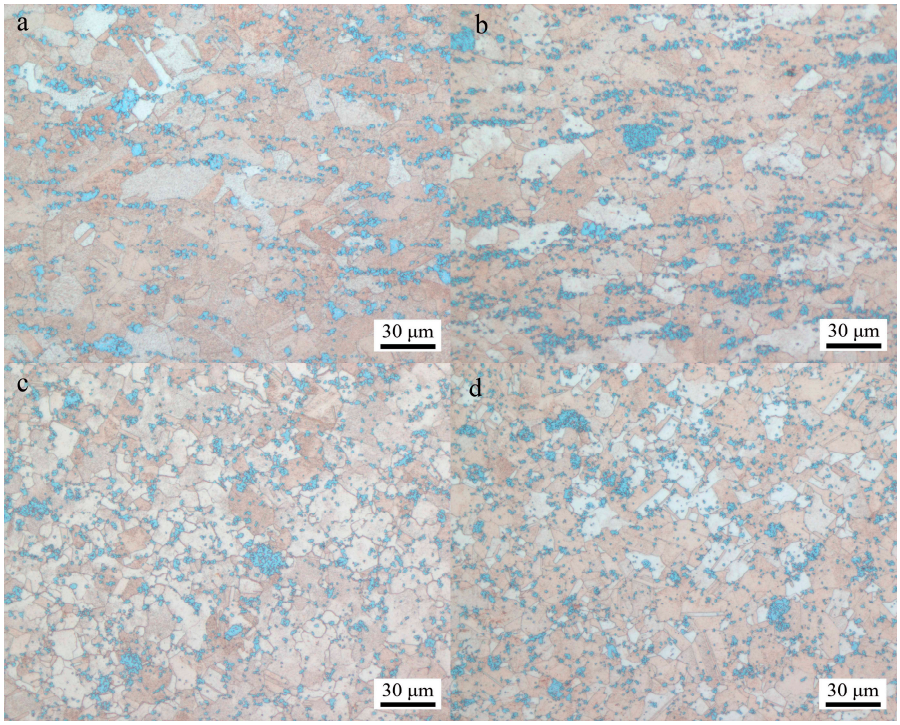


Figure 4. Microstructure of Cu-10wt%Mo composite at 900°C with different extrusion ratios: (**a**) 2.9; (**b**) 4.7; (**c**) 7.0; and (**d**) 10.5.

No abnormal grain growth is observed in the copper matrix of the Cu-10wt%Mo composite during hot extrusion. This is attributed to two factors: firstly, dynamic recrystallization occurring during the hot extrusion process refines the grains; secondly, the molybdenum phase embedded in the copper matrix inhibits grain growth, further contributing to grain refinement. During hot extrusion deformation of the Cu-10wt%Mo composite, the copper phase preferentially deforms and undergoes dynamic recrystallization, leading to the gradual disappearance of the original copper powder particle interfaces. Simultaneously, due to insufficient temperature and deformation, the molybdenum phase shows no significant deformation or recrystallization.

Figure 6 shows an image quality map (IQ) of Cu-10wt%Mo composite's microstructure, where it can be seen that the copper phases of composite materials with different extrusion ratios are all recrystallized grains accompanied by twin grains. The copper phase grains in the composite material with an extrusion ratio of 2.9 are coarser, and there are a small number of twin grains, as shown in Figure 6a. As the hot compression ratio increases, the copper phase grains in the composite material become finer, and the number of twin grains does not change significantly, as shown in Figure 6c,e. When the extrusion ratio continues to increase to 10.5, the number of twin grains in the microstructure of the composite material increases significantly, as shown in Figure 6g.

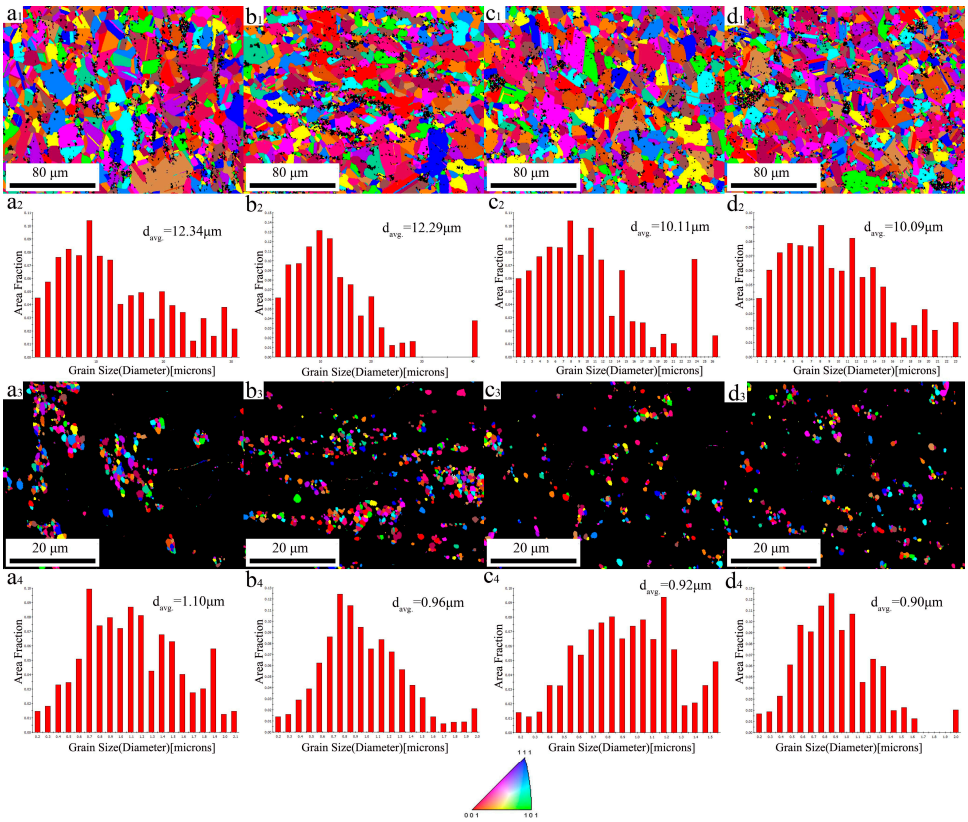


Figure 5. IPF diagram of Cu-10wt%Mo composite at 900°C with different extrusion ratios: (**a$_1$**–**a$_4$**) 2.9, (**b$_1$**–**b$_4$**) 4.7, (**c$_1$**–**c$_4$**) 7.0, and (**d$_1$**–**d$_4$**) 10.5.

During hot extrusion deformation, the copper powder particle interface in Cu-10wt%Mo composite greatly hinders the dislocation slip of the copper phase. At the same time, severe dislocation pile-up and localized stress concentration occur around the copper powder particle interface and molybdenum phase particles. As deformation proceeds, when the local stress exceeds the critical resolved shear stress (CRSS) for deformation twinning, twinning is initiated to accommodate the plastic strain and, thereby, relax the stress concentration in the Cu-10wt%Mo composite [21,22]. As the extrusion ratio increases, the powder particles are rapidly compacted, and the interfacial gaps between the powders become smaller, which, to some extent, reduces the difficulty of dislocation slip. At the same time, a larger extrusion ratio also increases the strain rate at the defect site. Therefore, the number of twin grains in composite materials with extrusion ratios of 4.7 and 7.0 is relatively stable. When the extrusion ratio continues to increase to 10.5, the strain rate at the defect site of the composite material sharply increases, triggering a large amount of twinning deformation and an increase in twinning.

Figure 6 also shows a geometrically necessary dislocation map (GND) of Cu-10wt%Mo composite's microstructure. GND map can reflect the dislocation distribution inside the grains and grain boundaries [23–25]. The dislocation density in most regions of the copper phase of Cu-10wt%Mo composite with different hot extrusion ratios is relatively low, as shown in the blue area of the microstructure GND map in Figure 6. Regions with higher dislocation densities are also present within the copper phase, represented by the green areas in the GND map. The highest dislocation density, storing high strain energy, is observed around the molybdenum phase particles, indicated by the white areas in the GND map. As the extrusion ratio increases, dynamic recrystallization becomes more complete, leading to a reduction in dislocation density within the copper phase. This is evidenced by the significantly reduced white and green areas in the GND map of the composite material

with an extrusion ratio of 7 (Figure 6f). However, when the extrusion ratio further increases to 10.5, the accumulated strain energy cannot be dissipated efficiently, causing a sharp increase in dislocations within the copper phase. Consequently, the green areas in the GND map of the composite material with an extrusion ratio of 10.5 increase noticeably (Figure 6h). The mutual insolubility between molybdenum and copper in the Cu-10wt%Mo composite results in stable phase interfaces and a high dislocation density during hot deformation across different extrusion ratios. Therefore, the white areas in the GND maps of the composite material microstructure shown in Figure 6 remain relatively stable.

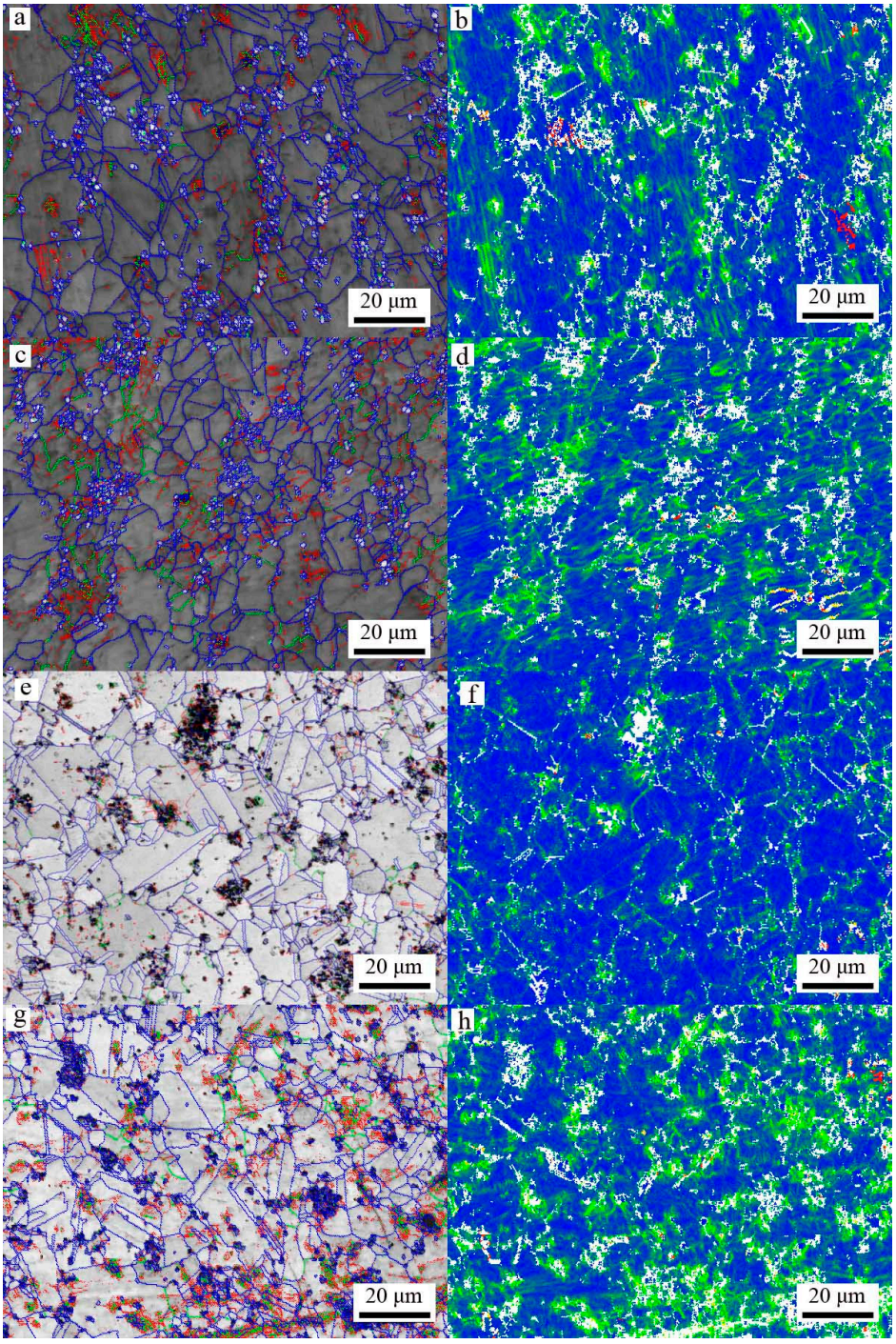


Figure 6. IQ map ((**a**) 2.9; (**c**) 4.7; (**e**) 7.0; (**g**) 10.5) and GND map ((**b**) 2.9; (**d**) 4.7; (**f**) 7.0; (**h**) 10.5) of Cu-10wt%Mo composite with different extrusion ratios at 900 °C.

Figure 7 shows the microstructure of Cu-10wt%Mo composite obtained by hot extrusion deformation at temperatures of 800, 850, 900, and 950 °C, with an extrusion ratio of 7.0. The microstructure IPF diagram of Cu-10wt%Mo composite under different extrusion temperatures is shown in Figure 8, where different colored regions represent different grain orientations. The numbers 1 and 2 in the figure sequence represent the copper phase grains and statistical graphs of the matrix, while the numbers 3 and 4 in the figure sequence represent the molybdenum phase grains and statistical graphs. Observation of Figures 7 and 8 reveals that, at an extrusion temperature of 800 °C, the copper phase grains in the composite material are non-uniform in size, indicating incomplete dynamic recrystallization. When the extrusion temperature increases to 850 °C, the copper phase undergoes preliminary dynamic recrystallization without the presence of excessively large grains, exhibiting an average grain size of 12.04 μm (Figure 8(b_2)). As the extrusion temperature further rises to 900 °C, the copper phase grains become fine and uniform with smooth, polygonal grain boundaries, showing an average grain size of 10.11 μm (Figure 8(c_2)). This suggests that complete dynamic recrystallization of the copper matrix occurs during hot extrusion at 900 °C. When the extrusion temperature reaches 950 °C, certain grains in the copper phase undergo significant growth, resulting in an average grain size of 11.80 μm (Figure 8(d_2)). Throughout hot extrusion at different temperatures, the molybdenum phase shows no noticeable deformation elongation and maintains an average grain size of approximately 1 μm (Figure 8(a_4–d_4)).

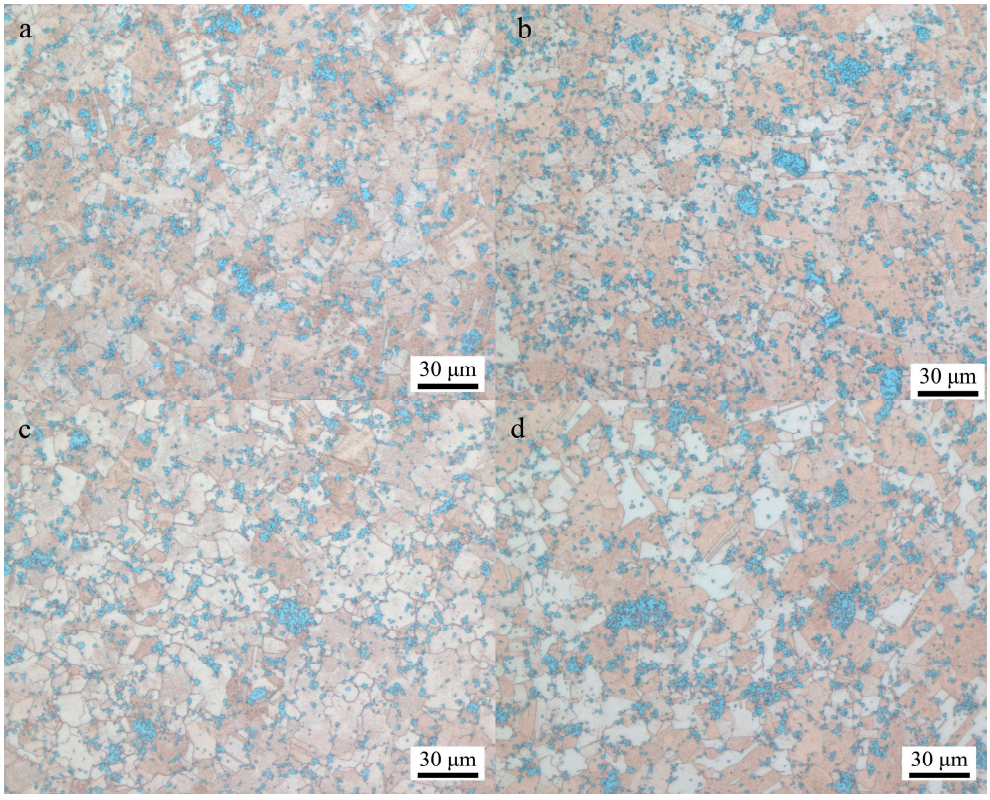


Figure 7. Microstructure of Cu-10wt%Mo composite with different extrusion temperatures: (**a**) 800 °C; (**b**) 850 °C; (**c**) 900 °C; and (**d**) 950 °C.

Figure 9 shows the microstructural IQ map and GND map of Cu-10wt%Mo composite after extrusion deformation at different temperatures. From Figure 9, it can be observed that dynamic recrystallization had occurred in the copper phase of all the extruded composite material. The composite material deformed at an extrusion temperature of 800 °C exhibited a higher density of twin grains, as shown in Figure 9a. As the temperature increased, the

copper phase grains in the composite materials hot-deformed at 850 °C and 900 °C became relatively finer, with small numbers of twin grains still present, as seen in Figure 9c,e. The microstructure of the composite material extruded at 950 °C consisted of coarse grains, while a limited number of twin grains remained, as illustrated in Figure 9g.

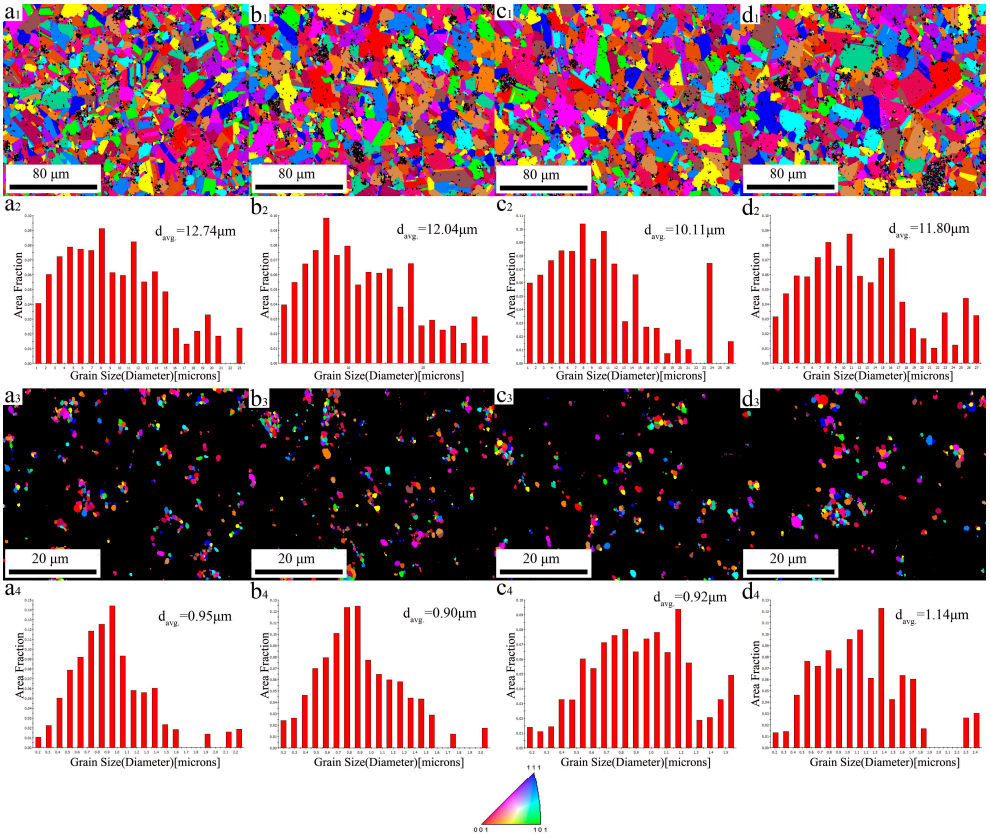


Figure 8. IPF diagram of Cu-10wt%Mo composite with different extrusion temperatures: (**a$_1$**–**a$_4$**) 800 °C, (**b$_1$**–**b$_4$**) 850 °C, (**c$_1$**–**c$_4$**) 900 °C, and (**d$_1$**–**d$_4$**) 950 °C.

At lower deformation temperatures, the driving force for grain boundary migration is low, and the powder particle interfaces lead to an increased local strain rate within the composite material's microstructure, resulting in the formation of excessive twins. As the hot extrusion temperature rises, the nucleation rate for recrystallization increases, and the driving force for grain boundary migration is enhanced. This promotes dynamic recrystallization, leading to the formation of finer recrystallized grains and a reduction in the number of twins. When the extrusion temperature is further increased to 950 °C, the composite material's microstructure undergoes complete recrystallization, followed by grain growth.

In the Cu-10wt%Mo composite after extrusion at different temperatures, most regions of the copper phase exhibit low dislocation density, represented by the blue areas in the GND map of the microstructure in Figure 9. However, regions with higher dislocation density are also present within the copper phase, shown as green areas in the GND map. The highest dislocation density is observed around the molybdenum particles, indicated by the white areas in the GND map. As the extrusion temperature increases, dynamic recrystallization becomes more complete, leading to a reduction in dislocation density within the copper phase. This is evidenced by the significantly reduced white areas in the GND map of the composite material extruded at 900 °C (Figure 9f). When the extrusion temperature is further increased to 950 °C, the recrystallized grains in the copper phase coarsen, and dislocations slip towards the Mo particle interfaces. This leads to an

increased local dislocation density, resulting in a renewed increase in white areas in the GND map (Figure 9h). The Cu-10wt%Mo composite features stable phase interfaces, and the deformation temperature remains below the recrystallization temperature of the molybdenum phase. Consequently, a high density of dislocations accumulates at these phase interfaces during hot extrusion, forming the white regions observed in the microstructural GND map.

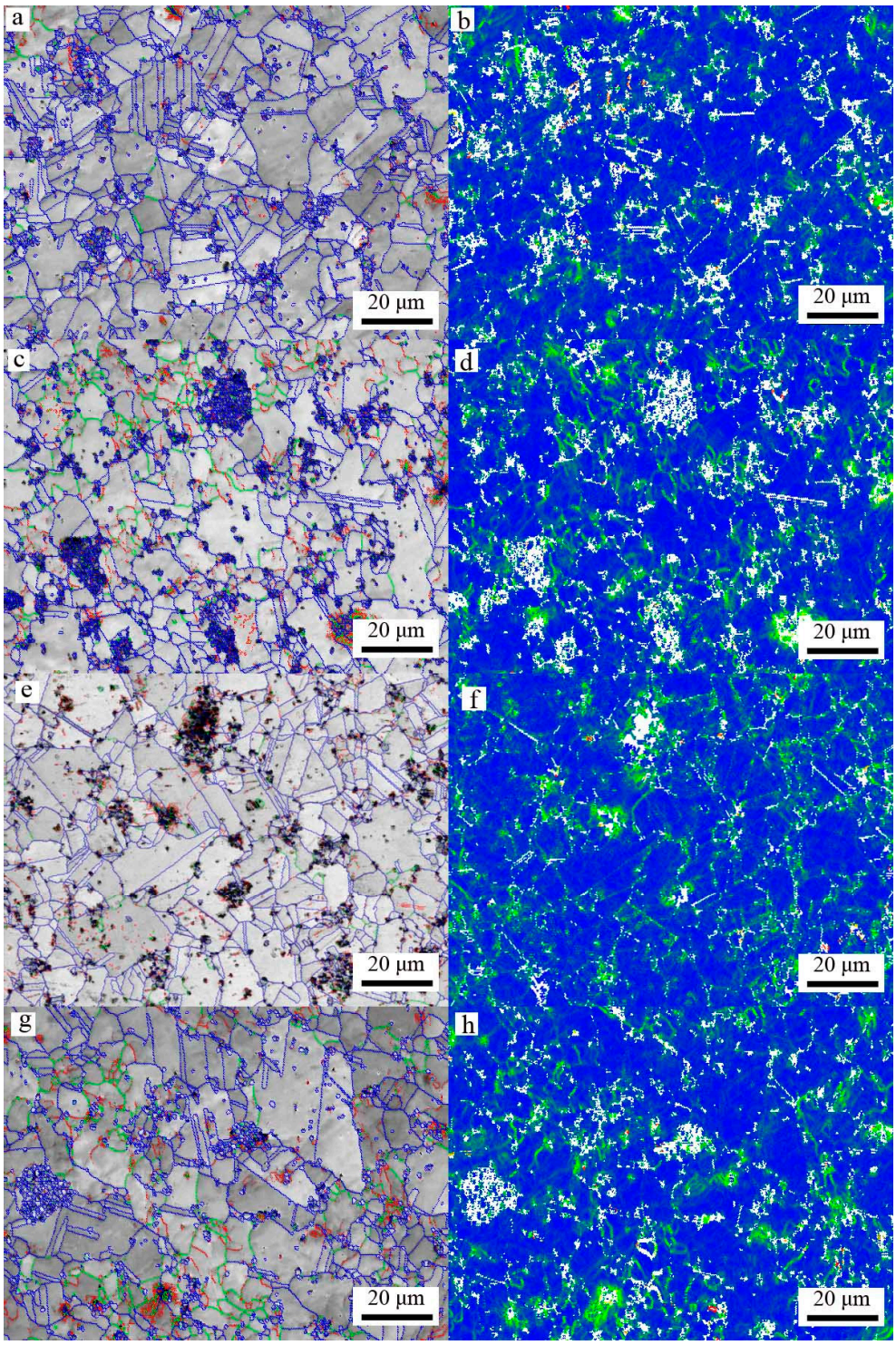


Figure 9. IQ map ((**a**) 800 °C; (**c**) 850 °C; (**e**) 900 °C; (**g**) 950 °C) and GND map ((**b**) 800 °C; (**d**) 850 °C; (**f**) 900 °C; (**h**) 950 °C) of Cu-10wt%Mo composite with different extrusion temperatures.

3.2. Tensile Mechanical Properties

Room-temperature tensile tests were conducted on Cu-10wt%Mo composites processed at 900 °C with different extrusion ratios, and the corresponding mechanical properties are shown in Figure 10. Comparative analysis revealed that the ultimate tensile strength (UTS) of the extruded rods with different extrusion ratios generally fell within the range of 250 MPa to 276 MPa. Among them, the composite material with an extrusion ratio of 7 exhibited the highest UTS, 276 MPa. Regarding yield strength, the rod with an extrusion ratio of 4.7 showed the highest value, approximately 157 MPa. Furthermore, comparison of the elongation after fracture indicated that the composite material with an extrusion ratio of 7.0 possessed a relatively high elongation, 29%. In summary, with the increase in the extrusion ratio, the ultimate tensile strength and elongation of the Cu-10wt%Mo composite first increased and then decreased. Based on the analysis of the composite material's microstructure, it can be concluded that the Cu-10wt%Mo composite with an extrusion ratio of 7.0 exhibits the most favorable overall performance.

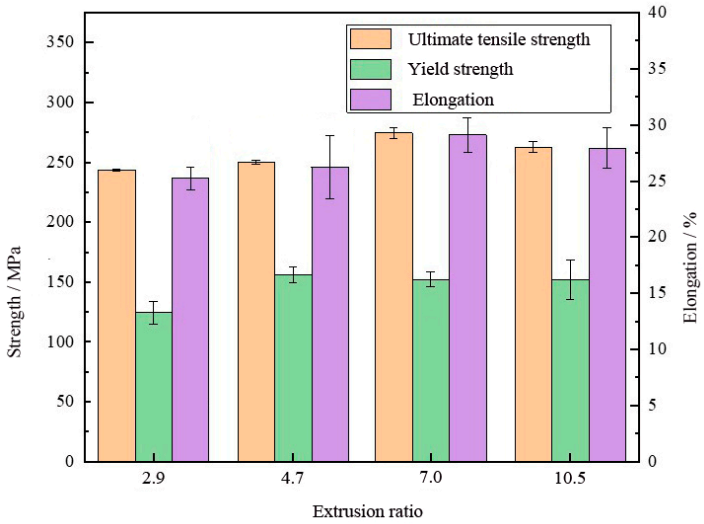


Figure 10. Room-temperature mechanical properties of Cu-10wt%Mo composite under constant extrusion temperature with varying extrusion ratios.

Room-temperature tensile tests were conducted on Cu-10wt%Mo composites extruded at different temperatures (800 °C, 850 °C, 900 °C, and 950 °C), and the corresponding mechanical properties are presented in Figure 11. Comparative analysis reveals that, as the extrusion temperature increases, the elongation after fracture of the Cu-10wt%Mo composite extruded rods shows an upward trend. This indicates improved plasticity, making the material more suitable for subsequent plastic deformation processing. However, when considering the ultimate tensile strength and yield strength values, it is noted that the yield strength of the composite material extruded at 950 °C decreases. This reduction is attributed to excessive extrusion temperature causing grain growth in the copper phase, thereby weakening the mechanical properties to some extent. Consequently, it is determined that the Cu-10wt%Mo composite extruded at 900 °C possesses the optimal combination of overall mechanical properties.

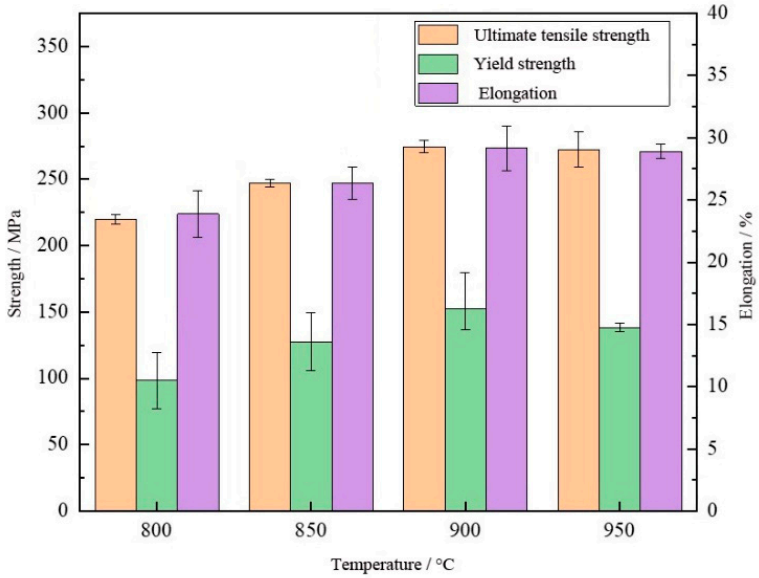


Figure 11. Comparison of room-temperature tensile properties of Cu-10wt%Mo composite extruded with a constant ratio of 7.0 at different temperatures.

3.3. Thermal Conductivity

Table 1 presents the thermal conductivity values of the Cu-10wt%Mo composite under different extrusion ratios. The composite material with an extrusion ratio of 7.0 exhibits a relatively high thermal conductivity, 369 W/(m·K). As the extrusion ratio increases, the thermal conductivity of the Cu-10wt%Mo composite first increases and then decreases.

Table 1. Thermal conductivity values of Cu-10wt%Mo composite under different extrusion ratios.

Extrusion ratio	2.9	4.7	7.0	10.5
Thermal conductivity value (W/(m·K))	349	354	369	358

Table 2 presents the thermal conductivity values of the Cu-10wt%Mo composite processed at different extrusion temperatures. As the extrusion temperature increases, the thermal conductivity of the Mo10Cu90 extruded rods shows an upward trend. The composite materials extruded at 900 °C and 950 °C both exhibit relatively high thermal conductivity, reaching 369 W/(m·K). This indicates that hot extrusion at these two temperatures results in higher material density, enabling the formation of interconnected thermal conduction pathways and, thereby, reducing the detrimental effect of pores on heat transfer. Although the thermal conductivity of the Cu-10wt%Mo composite gradually increases with rising hot extrusion deformation temperature, it stabilizes after reaching 900 °C.

Table 2. Thermal conductivity values of Cu-10wt%Mo composite at different extrusion temperatures.

Extrusion temperature	800 °C	850 °C	900 °C	950 °C
Thermal conductivity value (W/(m·K))	346	353	369	368

As a composite material, the theoretical thermal conductivity (Q_T) of a fully dense Cu-10wt%Mo composite can be calculated using the model proposed by Randall M. [26], as follows:

$$Q_T = Q_1 + Q_2 + Q_3 \quad (1)$$

where Q_1, Q_2, and Q_3 represent the thermal conductivity values of the Cu phase, Mo phase, and the Cu-Mo-Cu path, respectively. They can be obtained using the following expressions:

$$Q_1 = \pi R^2 Q_{Cu} \quad (2)$$

$$Q_2 = (1 - 2R)^2 Q_{Mo} \quad (3)$$

$$Q_3 = (Q_{Cu} Q_{Mo} A_L)/((3 R Q_{Mo}/2) + (1 - 3 R/2) Q_{Cu}) \quad (4)$$

In the expressions above, Q_{Cu} (403 W/(m·K)) and Q_{Mo} (139 W/(m·K)) are the theoretical thermal conductivities of copper (Cu) and molybdenum (Mo), respectively [27]. A_L represents the area of the copper wetting layer, and R is a constant. The value of R can be calculated using the volume fraction φ_{Cu} of copper. The parameters A_L and R are given by the following two expressions:

$$A_L = 4R(1 - R) - \pi R^2 \quad (5)$$

$$R = 0.0113 + 1.58 \varphi_{Cu} - 1.83 \varphi_{Cu}^{3/2} + 1.06 \varphi_{Cu}^{3} \quad (6)$$

The fully dense theoretical thermal conductivity of the Cu-10wt%Mo composite, calculated using Equations (1)–(6), is 378 W/(m·K).

The thermal conduction in metallic materials is primarily governed by lattice vibrations (phonons) and electron transport [28–34]. The Cu-10wt%Mo composite, with a copper content of 90 wt%, exhibits a continuous copper matrix that acts as the dominant thermal conduction pathway. Recrystallization occurring during hot extrusion deformation eliminates the original inter-particle boundaries of copper powders, replacing them with recrystallized grain boundaries within the copper phase. The interfaces between the original copper powder particles typically contain numerous defects, such as pores and impurities. In contrast, the boundaries of the recrystallized copper grains have significantly fewer defects. This reduction in defects diminishes their scattering effect on lattice waves (phonons), leading to an increased mean free path of phonons and enhanced atomic vibrations, thereby improving thermal conductivity [35,36]. On the other hand, the reduced defect density also decreases the obstruction to electron motion. The enhanced electron transport further contributes to the increase in thermal conductivity. Consequently, the extruded Cu-10wt%Mo composite exhibits high thermal conductivity. Notably, the composite material extruded at 900 °C with an extrusion ratio of 7.0 achieves a thermal conductivity as high as 369 W/(m·K), which is very close to the theoretical value. Simultaneously, the molybdenum phase in the extruded Cu-10wt%Mo composite does not undergo recrystallization and remains in the form of original molybdenum particles. The interfaces between these molybdenum particles impede thermal conductivity to some extent, resulting in the failure of the extruded composite material to achieve the theoretical thermal conductivity of its fully dense counterpart.

4. Conclusions

The high temperature and pressure generated during hot extrusion deformation cause further shrinkage and closure of pores on the surface of original powder particles in the as-sintered Cu-10wt%Mo composite. This results in complete metallurgical bonding between the copper powder particles, promotes atomic diffusion, eliminates the original interfaces of copper powder particles, and thereby enhances the density of the material.

During the hot extrusion process, the copper phase in the Cu-10wt%Mo composite undergoes dynamic recrystallization without exhibiting abnormal grain growth. The primary reasons are twofold: firstly, dynamic recrystallization inherently refines the grain

structure; secondly, the molybdenum phase embedded within the copper matrix inhibits grain growth, thereby further contributing to grain refinement.

The formation of a considerable number of twins in the copper phase of Cu-10wt%Mo composite during hot extrusion is primarily attributed to the significantly higher strain rate in the copper phase around molybdenum particles compared to the average level. This localized strain concentration consequently induces twin formation during the dynamic recrystallization process.

The Cu-10wt%Mo composite processed by hot extrusion with a ratio of 7.0 at 900 °C exhibits excellent mechanical properties and high thermal conductivity, with an ultimate tensile strength of 276 MPa, an elongation at break of 29%, and a thermal conductivity of 369 W/(m·K).

Hot extrusion deformation at temperatures below 950 °C fails to achieve complete metallurgical bonding of the molybdenum phase in the Cu-10wt%Mo composite. The residual original powder particle interfaces and pores exert negative impacts on the densification process, thereby limiting further enhancement of both mechanical properties and thermal conductivity.

Author Contributions: Q.L.: conceptualization, methodology, writing—original draft preparation, writing—review and editing, and visualization. Z.L.: validation, formal analysis, and project administration. Z.Z.: validation, investigation, and data curation. S.H.: conceptualization, validation, data curation, and writing—review and editing. All authors have read and agreed to the published version of the manuscript.

Funding: This research received no external funding.

Data Availability Statement: The original contributions presented in this study are included in the article. Further inquiries can be directed to the corresponding author.

Conflicts of Interest: Author Qing Li is employed by the companies GRINM Group Co., Ltd and GRIMAT Engineering Institute Co., Ltd. Authors Zengde Li, Zhanning Zhang and Songxiao Hui are employed by company GRIMAT Engineering Institute Co., Ltd. The authors declare that the research was conducted in the absence of any commercial or financial relationships that could be construed as a potential conflict of interest.

Abbreviations

The following abbreviations are used in this manuscript:

EMAX Energy-Dispersive X-ray Microanalysis System

References

1. Ji, X.P.; Cao, W.C.; Bu, C.Y.; He, K.; Wu, Y.D.; Zhang, G.H. A new route for preparing Mo-10wt.%Cu composite compacts. *Int. J. Refract. Met. Hard Mater.* **2019**, *81*, 196–205. [CrossRef]
2. Li, Q.; Li, Z.D.; Xie, H.F.; Peng, L.J.; Mi, X.J. Microscopic formation mechanism and physical properties of Mo/Cu composites with high densification. *Mater. Sci. Forum.* **2023**, *1094*, 35–44. [CrossRef]
3. Hu, X.; Hu, H.; Lai, R.M.; Xie, Q.C.; Zhi, Y. Cyclic warm rolling: A path to superior properties in Mo-Cu composites. *Int. J. Refract. Met. Hard Mater.* **2025**, *126*, 106926. [CrossRef]
4. Zhu, Z.X.; Ren, X.J.; Jin, K.J.; Tan, H.; Zhu, S.Y.; Cheng, J.; Guo, J.; Yang, J. Current-carrying tribological properties and wear mechanisms of Mo-containing Cu alloy coatings produced by laser cladding. *Tribol. Int.* **2024**, *200*, 110107. [CrossRef]
5. Hu, W.Q.; Wei, L.F.; Li, Y.C.; Zhang, W.; Ma, Z.Q.; Liu, C.X.; Liu, Y.C. Phase interface engineering: A new route towards ultrastrong yet ductile Mo alloy. *Mater. Sci. Eng. A* **2024**, *889*, 145867. [CrossRef]
6. Wang, D.Z.; Chen, D.D.; Yang, Y.H.; Sun, A.K. Interface of Mo-Cu laminated composites by solid-state bonding. *Int. J. Refract. Met. Hard Mater.* **2015**, *51*, 239–242. [CrossRef]
7. Fang, F.; Zhou, Y.Y.; Yang, W. Temperature dependent tensile and fracture behaviors of Mo-10 wt.% Cu composite. *Int. J. Refract. Met. Hard Mater.* **2014**, *42*, 120–125. [CrossRef]

8. Jin, Z.L.; Li, P.P.; Zheng, B.; Xiao, D.D. The structure and properties of electroless Ni-Mo-Cr-P coatings on copper alloy. *Mater. Corros.* **2013**, *64*, 341–346. [CrossRef]
9. Paola, A.B.; Benjamin, S.; Rodrigo, H.P. Liquid phase sintering of mechanically alloyed Mo-Cu powders. *Mater. Sci. Eng. A* **2017**, *701*, 237–244. [CrossRef]
10. Minasyan, T.; Kirakosyan, H.; Aydinyan, S.; Liu, L.; Kharatyan, S.; Hussainova, I. Mo-Cu pseudoalloys by combustion synthesis and spark plasma sintering. *J. Mater. Sci.* **2018**, *53*, 16598–16608. [CrossRef]
11. Ye, L.; Tian, N.; Zhang, C.; Guan, J.; Wan, H.; Guan, Q. Surface Alloying on Cu with Mo by High-Current Pulsed Electron Beam Irradiation. *Chin. J. Vac. Sci. Technol.* **2024**, *44*, 258–265.
12. Xu, Y.; Wang, S.; Gao, Y.; You, L.; Pang, X.; Lu, H.; Song, C.; Zhang, Y. Improving the mechanical and tribological properties of Cu matrix composites by doping a Mo2BC ceramic. *J. Alloys Compd.* **2024**, *1009*, 177003. [CrossRef]
13. Kim, S.; Yoon, H.W.; Moon, K.I.; Lee, C.S. Mechanical and friction behavior of sputtered Mo-Cu-(N) coatings under various N2 gas flow using a multicomponent single alloy target. *Surf. Coat. Technol.* **2021**, *412*, 127060. [CrossRef]
14. Liu, T.Y.; Liu, X.W.; Cao, J.; Feng, X.Y.; Li, S.K.; Liu, J.X. Amorphous interlayer assisted ductility of Mo-Cu alloy. *Mater. Des.* **2023**, *231*, 112010. [CrossRef]
15. Du, J.L.; Huang, Y.; Xiao, C.; Liu, Y.C. Building metallurgical bonding interfaces in an immiscible Mo/Cu system by irradiation damage alloying (IDA). *J. Mater. Sci. Technol.* **2018**, *34*, 689–694. [CrossRef]
16. Yang, H.M.; Zhang, M.; Li, G.; Bai, W.W.; Huang, Y.D. Extrusion temperature dependence of microstructure and mechanical behavior for a lightweight Mg-7Li-3Al-0.3Si-0.3Mn dual-phase alloy. *J. Alloys Compd.* **2025**, *1046*, 184946. [CrossRef]
17. Qin, X.B.; Jia, C.Y.; Yang, Q.; Dai, C.; Feng, W.Z.; Wu, W.Q. Multi-objective optimization design and verification of extrusion die structure for TC4 titanium alloy Y-section profile. *J. Mater. Res. Technol.* **2025**, *39*, 1585–1598. [CrossRef]
18. Bagliuk, G.A.; Kyryliuk, S.F. Evolution of the stress-strain state of porous workpieces in hot extrusion forging to produce axisymmetric parts with an axial hole. *Powder Metall. Met. Ceram.* **2023**, *61*, 504–513. [CrossRef]
19. *GB/T 228.1-2021*; Metallic Materials-Tensile Testing–Part 1: Method of Test at Room Temperature. Standards Press of China: Beijing, China, 2021.
20. *GB/T 22588-2008*; Determination of Thermal Diffusivity or Thermal Conductivity by the Flash Method. Standards Press of China: Beijing, China, 2008.
21. Yako, S.; Park, M.; Tsuji, N. Quantitative evaluation of local strain distribution induced by deformation twins and triggering effect of deformation twinning on neighboring grains in polycrystalline AZ31 magnesium alloys. *Scr. Mater.* **2025**, *255*, 116388. [CrossRef]
22. Yang, J.K.; Zhang, J.Y.; Liu, G.; Sun, J. Sequentially-activated multiple deformation mechanisms enable a hierarchically duplex titanium alloy with high strength-ductility synergy. *Acta Mater.* **2025**, *301*, 121546. [CrossRef]
23. Field, D.P.; Trivedi, P.B.; Wright, S.I.; Kumar, M. Analysis of local orientation gradients in deformed single crystals. *Ultramicroscopy* **2005**, *103*, 33–39. [CrossRef]
24. Jiang, Z.W.; Yin, D.D.; Wan, Y.F.; Ni, R.; Zhou, H.; Zhang, J.; Wang, Q.D. Slip system activation and plastic strain heterogeneity in compressed Mg-10Gd-3Y-0.5Zr alloy. *Trans. Nonferrous Met. Soc. China.* **2023**, *33*, 79–94. [CrossRef]
25. Zhong, H.; Shi, Q.; Dan, C.; You, X.; Zong, S.; Zhong, S.; Zhang, Y.; Wang, H.; Chen, Z. Resolving localized geometrically necessary dislocation densities in Al-Mg polycrystal via in situ EBSD. *Acta Mater.* **2024**, *279*, 120290. [CrossRef]
26. German, R.M. A model for the thermal properties of liquid-phase sintered composites. *Metall. Mater. Trans. A* **1993**, *24*, 1746–1752. [CrossRef]
27. Ke, S.X.; Feng, K.Q.; Zhou, H.L.; Shui, Y. Phase evolution of Mo-W-Cu alloy rapid prepared by spark plasma sintering. *J. Alloys Compd.* **2019**, *775*, 784–789. [CrossRef]
28. Azemian, S.; Fanchini, G. Electron-phonon interaction and lattice thermal conductivity from metals to 2D Dirac crystals: A review. *J. Phys. Condens. Matter* **2025**, 1–31. [CrossRef]
29. Wang, A.; Sheng, Y.F.; Bao, H. Recent advances in thermal transport theory of metals. *Acta Phys. Sin.* **2024**, *73*, 037201. [CrossRef]
30. Lepeshkin, A.R.; Vaganov, P.A. Investigations of thermal conductivity of metals in the field of centrifugal and vibration accelerations. *J. Phys. Conf. Ser.* **2016**, *774*, 012022. [CrossRef]
31. Xia, Y.L.; Zhang, X.Y.; Wang, A.; Sheng, Y.F.; Xie, H.; Bao, H. Critical factors influencing electron and phonon thermal conductivity in metallic materials using first-principles calculations. *J. Phys. Condens. Matter* **2024**, *37*, 055701. [CrossRef]
32. Herzog, M.; Reppert, A.; Pudell, J.; Henkel, C.; Kronseder, M.; Back, C.H.; Maznev, A.A.; Bargheer, M. Phonon-dominated energy transport in purely metallic heterostructures. *Adv. Funct. Mater.* **2022**, *32*, 055701. [CrossRef]
33. Peng, J.; Deskins, W.R.; Braga, M.H.; El-Azab, A. Effect of electron-phonon coupling on thermal transport in metals: A Monte Carlo approach for solving the coupled electron-phonon Boltzmann transport equations. *AIP Adv.* **2025**, *15*, 025108. [CrossRef]
34. Karna, P.; Giri, A. Electron-electron scattering limits thermal conductivity of metals under extremely high electron temperatures. *J. Phys. Condens. Matter* **2024**, *36*, 185701. [CrossRef]

35. Ye, X.B.; He, Z.H.; Pan, B.C. The thermal conductivity of defected copper at finite temperatures. *J. Mater. Sci.* **2019**, *55*, 4453–4463. [CrossRef]
36. Chang, G.; Zhang, S.; Chen, K.Y.; Zhang, W.; Li, L.; Zhang, Y.J.; Peng, H.R.; Kan, D.X.; Wang, L.H.; Zhang, H.L.; et al. Achieving excellent thermal transport in diamond/Cu composites by breaking bonding strength-heat transfer trade-off dilemma at the interface. *Compos. B Eng.* **2025**, *289*, 111925. [CrossRef]

Disclaimer/Publisher's Note: The statements, opinions and data contained in all publications are solely those of the individual author(s) and contributor(s) and not of MDPI and/or the editor(s). MDPI and/or the editor(s) disclaim responsibility for any injury to people or property resulting from any ideas, methods, instructions or products referred to in the content.